10TH INTERNATIONAL SYMPOSIUM ON PARTICLE IMAGE VELOCIMETRY - PIV13
Delft, The Netherlands, July 1-3, 2013

Three-Dimensional Flow Field Investigations on Pitching Low Aspect Ratio Wings at Low Reynolds Numbers

Hauke Ehlers[1], Janos Agocs[1], Robert Konrath[1], Ivan Korkischko[1], Daniel Schanz[1], Reinhard Geisler[1], Christian Willert[2] and Ralf Wokoeck[3]

[1] Institute of Aerodynamics and Flow Technology, German Aerospace Center (DLR), G öttingen, Germany
Hauke.Ehlers@dlr.de

[2] Institute of Propulsion Technology, German Aerospace Center (DLR), Cologne, Germany
[3] Institute of Fluid Mechanics, Technische Universit ät Braunschweig, Braunschweig, Germany

ABSTRACT

Three-dimensional, unsteady flow fields of a pitching low aspect ratio wing were measured by tomographic PIV [6] in air. The analysis of the vortex dominated flow field provides a deeper understanding of vortex interaction and three-dimensionality of the low Reynolds number ($Re \approx 10,000$) flow. In order to recover the complete flow field the measurement set-up was designed to be traversable. A high spatial resolution and a large volume thickness could be achieved by a set of high sensitive sCMOS cameras. A specific feature of this campaign was to locate the measurement domain directly above the flat-plate-wing surface. Evaluation of the measurement data is performed by DLR in-house software. A selection of measurement results of this highly complex flow is presented in this paper.

1. Introduction

As the performance of stationary airfoils deteriorates rapidly if the Reynolds number decreases below $Re = 100,000$ [1], the flapping flight is seen as an efficient method for wings operating to produce lift and thrust at low Reynolds numbers. This is motivated by the flight mechanisms used of birds and insects in nature. The mechanism for providing high lift coefficients in low Reynolds number domain is thought to be largely influenced by the formation of vortices. Flow field studies on insects [2] for example show how additional lift can be produced by generating a large leading edge vortex (LEV) that produces an additional suction on the wing surface. This example shows the importance of the flow topology in flapping flight especially at low Reynolds numbers. In case of low aspect ratio (*AR*) wings, complex three-dimensional flows develop, which are considered by Visbal et al. [3] for heaving wings by performing both numerical and experimental investigations on an $AR = 2$ rectangular flat plate. An intense transverse flow towards the wing center line caused by the leading edge vortex is found and a detachment of this LEV from the front corners of the plate forming an arch-type structure above the wing. Apart from flow investigations on wings performing simplified periodical motions also transient cases are of interest for a deeper understanding of the instantaneous aerodynamics. Jantzen et al. [4] performed numerical simulations to investigate the vortex dynamics of a low *AR* plate wing. The Reynolds number, *AR* and the pitch rate have been varied to understand the effect of a pitch-up manoeuvre pivoting about the leading edge. They observed similar features for the vortex structure at different Reynolds numbers ($Re = 50$, 100, 300, 500) with respect to the LEV, trailing edge vortex (TEV), and tip vortex. However, for higher Reynolds numbers the vortices seem to become more instable. Furthermore they observed a greater effect on the forces and vortex dynamics generated during the pitching motion for varying the aspect ratio ($AR = 1$, 2, 4). For smaller *ARs* the tip effects on the wing center increase. A similar pitch-up manoeuvre has been investigated experimentally for an aspect ratio 4 wing by Stevens et al. [5] at $Re = 10,000$. They performed a uniform acceleration at 0° incidence followed by a fast respectively a slow pitch while pivoting about the mid-chord. A combination of dye flow visualisation technique and 2-D PIV measurement have been used to study the influence on the LEV. They conclude, that a fast pitch manoeuvre forms a classical LEV which dominates the flow while slow pitch-up forms a largely separated flow.
Quantitative experimental 3-D results for large amplitude pitch-up motions would allow for a better understanding of vortex dynamics of this manoeuvre. In the present paper tomographic PIV has been applied to a canonical pitch-up manoeuvre allowing for a detailed study of the three-dimensional flow development at specific phase angles of the motion; e.g. particularly in regard to the interaction between the tip vortices and the flow separation and leading edge vortex.

2. Experimental Procedure

2.1 Wind Tunnel Facility

The experiment was conducted in the MAV-Lab experimental facility at the Institute of Fluid Mechanics of the Technische Universität Braunschweig. This facility was especially designed for low Reynolds number flow investigations. A schematic of the continuous atmospheric Eiffel-type wind tunnel facility is shown in Figure 1a. The test section is 1500 mm long with a 400×600 mm^2 cross-section and has transparent side walls and ceiling for optical access. The low perturbation incoming flow is characterized by a turbulence level of less than 0.1% at 10 m/s and a core velocity uniformity of 99%. The tunnel is driven in suction mode within the operational range of 2 to 20 m/s. The facility contains a dynamic model support which enables the model to perform movements with 2 degrees of

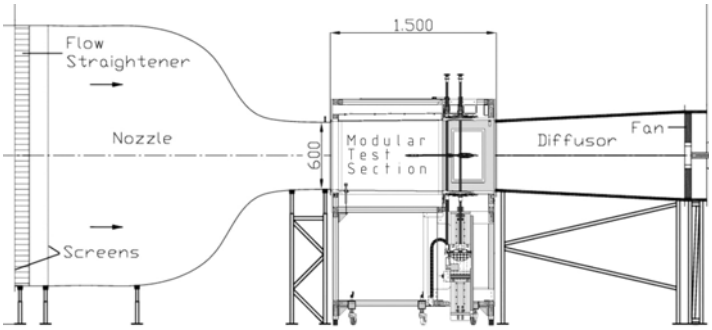

(a) LNB windtunnel for low Reynolds number investigations.

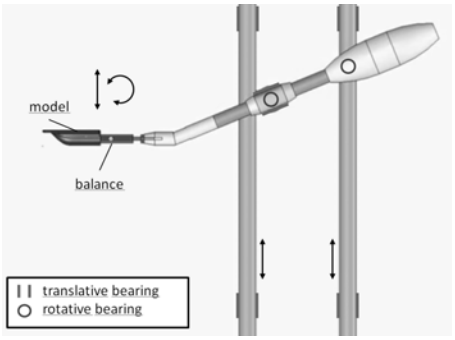

(b) Dynamic model support enables to perform instantaneous pitch and/or pitch-plunge motions.

Figure 1: Low Noise Windtunnel of the Institute of Fluid Mechanics and exchangeable test rig including the dynamic model support.

freedom (pitch and/or plunge). A schematic of the apparatus is shown in Figure 1b. Concerning the principle of actuation a rotational motion involves an additional motion component in incoming flow direction.

2.2 Wind Tunnel Model

A thin flat plate model of rectangular planform ($AR = 4$) has been manufactured. The model has a chord length of $c = 70$ mm, a thickness-to-chord ratio of 3.4% and rounded edges. A fuselage on the lower side of the plate covers the strain gauge balance which gives the connection to the dynamic model support. The width of the fuselage is $0.057b$. To reduce the weight and enhance the stiffness the wing model is made of carbon fibre reinforced plastic. It consists of a black high-gloss surface to minimize laser light scatter for optimal application of optical measurement techniques.

2.3 Pitching Kinematics

The initial condition of the pitch-up manoeuvre is 0° incidence and free stream velocity $U_\infty = 2.15$ m/s. If the convective time is defined by $t_c = c/U_\infty = 0.033$ s the pitch-up to $\alpha = 45^\circ$ (pivot about leading edge) shall be achieved within $t_{move} = 6t_c$. The linear ramp is approximated with a continuous function characterized by a wide range of linearity. Characteristic parameters for the manoeuvre are the Reynolds number $Re = U_\infty c/\nu \approx 10,000$ and the reduced frequency $k = \Delta\alpha/t_{move} \cdot c/(2U_\infty) = 0.065$.

2.4 Tomo PIV Set-up

Tomographic PIV measurements have been applied to capture the flow field above the wing. A schematic of the measurement set-up is shown in Figure 2. The set-up has been constructed in order to enable efficient variations of the measurement position and angle. Providing 400 mJ per pulse a high energy Nd:YAG laser (BigSky CFR) has been used to illuminate small DEHS tracer particles. The laser light volume dimensions have been ($h \times t = 50 \times 20$ mm^2). To capture the complete flow field above the wing with good spatial resolution, measurements are applied successively, scanning the flow field in a chordwise direction. The measurement domain between leading edge and $0.35c$ beyond trailing edge consists of six sub-volumes. The width of the measurement domain was about 120 mm starting $0.033b$ beyond the wing tip. Consequently, flow field data is not available between symmetry plane and $y_n \approx 0.5$ in spanwise direction. A system of four high resolution scientific CMOS cameras (PCO.edge: 2560×2160 pixel, 16 bit, max 25 Hz in double shutter mode) has been used to capture the illuminated DEHS particles from different directions. On each side of the test rig two cameras have been positioned (see Figure 3b). The optical axis of each camera has been aligned tangential to the model surface to avoid reflected particles in the recordings according to the polished high-gloss model surface. In order to obtain a fine adjustment of the camera and to ensure that the field of view is uniformly in focus, Scheimpflug adapters are used. A mirror was used to reflect the laser beam back and thus enhance the scattered light intensity for the backward facing cameras. The four cameras and the 45° tilted mirror have been mounted on high precision linear stages to enable for translating the measurement set-up in chordwise direction. Camera calibration has been applied to every of the six measurement positions to avoid de-calibration due to linear stages being out of alignment. Therefore the two-plane calibration plate was also mounted an a linear stage (see Figure 3a).
For triggering the correct phase of the pitch-up manoeuvre, two laser light barriers have been aligned with one of the linear motors of the model actuation mechanism. A sequencer was provided by the signal to control the laser and cameras. Another camera has been installed to capture the model in side-view and monitor its position and pitch angle to match the dynamic movement of the model to the fixed measurement set-up. For the volume self-calibration 100 image pairs have been recorded for each of the six chordwise positions using low seeding density. For the measurement a more intense seeding density was used. For this 150 image pairs per chordwise position have been recorded.

3. Evaluation Procedure

The complete evaluation of the measurement data is performed by DLR in-house software. The procedure is divided into three subroutines: The camera calibration (which includes volume self-calibration), reconstruction of the particle distribution and a 3-D cross-correlation routine.

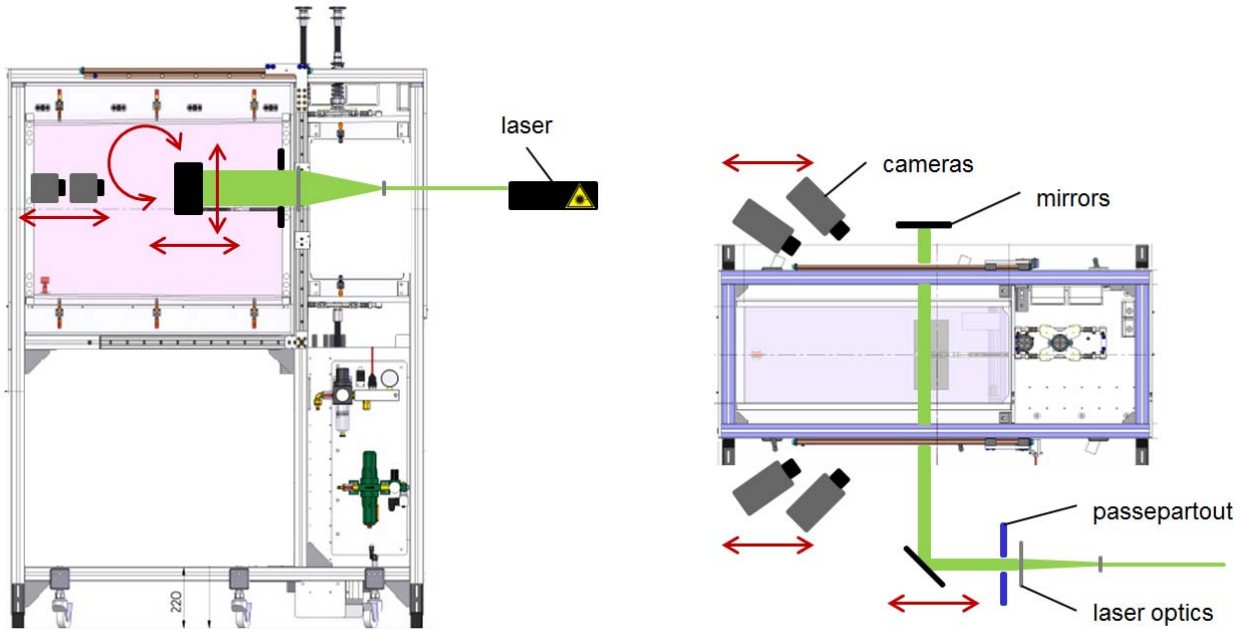

(a) Side view.

(b) Top view.

Figure 2: Schematic of tomographic PIV measurement set-up.

3.1 Camera Calibration

The camera system was calibrated for every of the six chordwise measurement positions using a two-plane calibration plate mounted on a high precision linear stage (see Figure 3a). To take the calibration plate out of the test section one of the glass side walls needs being opened and closed. This may have caused some vibrations to the camera set-up. Occurring deviations were corrected applying volume self-calibration [9] in two steps. At first low seeded images were used to calculate the main correction. Volume self-calibration was again applied to the high density measurement images to correct impreciseneses caused by moving the linear stages. Maximum overall errors of below 1.6 pixel were encountered despite the fact that the whole camera system was moved multiple times between optical calibration and the measurements. The calibration procedure offered the possibility to calibrate the average optical transfer function of the particles originating from different parts of the volume [11]. As, however, it was found that particle imaging was unproblematic, it was decided to omit the OTF-information in the reconstruction process in order to achieve maximum reconstruction speed.

3.2 Particle Reconstruction

Reconstruction of the particle distributions was done using a SMART algorithm with MLOS initialization [10, 11]. The thickness of the evaluated volume was reduced to 18 mm because of the decreasing intensity of the laser illumination near the volume borders. Figure 4 shows an intensity z-profile for a selected volume, illustrating the laser intensity profile and the particle-to-ghost intensity ratio. The ratio is about 1.4 and hence relatively low due to a reduction in voxel-to-pixel ratio. The voxel-to-pixel ratio was set to a value of 0.8, in order to allow an effective processing of the large amount of data. Vector results from these reduced reconstructions showed little difference to full reconstructions using a voxel-to-pixel ratio of 1.0. Using these settings, the evaluation domain of every volume is represented by a voxel-space of $912 \times 2177 \times 329$ voxel (resolution ≈ 18.2 voxel/mm). Five iterations of SMART were applied after the MLOS initialization. Reconstructing a double volume on a cluster with 16 cores requires ≈ 5 min.

3.3 Particle displacement estimation

The recovered volume pairs of three-dimensional particle distributions are then processed with a cross-correlation based displacement estimation algorithm. Just as in established 2-C processing schemes, the 3-D algorithm employs a resolution pyramid which starts at a rather coarse grid and stepwise increases resolution while continually updating a predictor field [15, 14]. Factor N image downsampling is achieved by summing $N \times N \times N$ adjacent voxels rather than only resampling the volume. At a given resolution level integer-based sample offsetting is applied in a symmetric fashion using the estimation from the previous resolution step [18, 17]. Intermediate validation is based on normalized median filtering as proposed by Westerweel & Scarano [19]. Once the desired final spatial resolution is reached volume deformation is applied at least twice to further improve the match between the volumes and thereby improving the displacement estimate. Volume deformation is based on B-spline interpolation as presented by Thévenaz et al. [13]. The main advantage of this family of interpolators is that they have superior interpolation quality even for rather short bases of 3 to 4 pixels and their separability allows very efficient computation. Further, for a given image or voxel data set the interpolation coefficients need only to be computed once and can be reused during the iterative image or volume deformation. The disadvantage is that the set of coefficients, the same size as the number of volume voxels has to be kept in memory. Even for sparsely populated data sets such as 3-D particle image distributions areas without image intensity variations have non-zero interpolation coefficients and hence the entire voxel space of coefficients must be kept in memory. While not implemented in the present case, significant interpolation speed can be

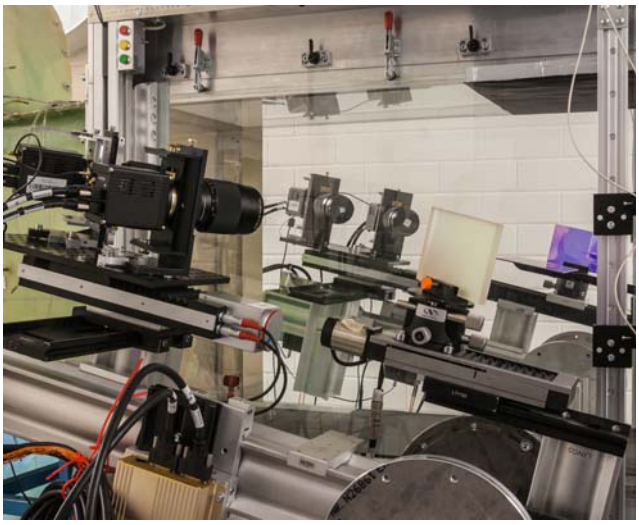

(a) Camera set-up and mirror arrangement on both sides of the test section; model on the right side.

(b) Calibration plate mounted an a linear stage inside the test section; 2 cameras in the front, 1 camera and a movable mirror in the background.

Figure 3: Pictures of the tomographic PIV measurement set-up.

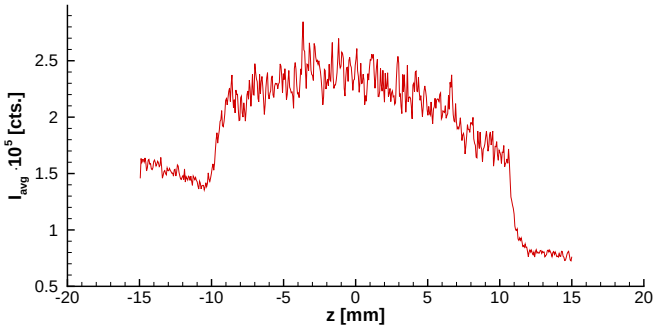

Figure 4: Intensity z-profile of a representative reconstructed volume; each z-value is an averaged pixel count of the related x-y-plane.

achieved by interpolating only the immediate neighborhood of particles [16]. The normalized cross-correlations are computed using the spectral approach via conjugate multiplication and highly optimized FFTs [20]. No direct correlation has been utilized here although the sparseness of voxel data suggest an additional speed increase, at the very least at the last iteration steps with displacements in the ± 1 voxel range [16]. Correlation peaks are searched within increasingly tight margins for each interrogation pass which are typically limited to a region of ± 2 to 3 voxel at the final resolution. Sub-pixel accurate peak location estimation via three-point Gauss fits along each principle direction is used making use of only 7 correlation values. More complex correlation peak fitting algorithms were not investigated here.
In the present application a three level resolution pyramid was used with a final window size of 48^3 voxel (75% overlap), resulting in vector volumes with $75 \times 175 \times 25$ nodes. At this resolution volume deformation was applied twice using a cubic B-spline of order 3. To achieve high processing speed the cross-correlation algorithm is thoroughly parallelized using OpenMP [12]. Computing one vector volume on a cluster with 16 cores requires ≈ 3 minutes.

4. Results

Two phases of the pitch-up manoeuvre have been measured and evaluated as described above, i.e. at a geometric angle of attack of $\alpha_{p1} = 22.5^\circ$ and $\alpha_{p2} = 30^\circ$. Referring to Jantzen et al. [4] water tunnel force measurements α_{p1} is close to the end of the linear segment of the lift slope and for α_{p2} maximal lift, C_L is reached. The resulting 3-D flow fields and selected 2D slices are illustrated in Figures 5 to 7. The completely evaluated measurement domain covers a volume starting close to the LE and ending $\approx 0.35c$ downstream the TE in cordwise direction. In spanwise direction the domain starts $0.5c$ outboard of the symmetry plane and ends $0.13c$ beyond the tip. The origin of the coordinate system is located in the symmetry plane of the wing at quarter chord position.
Figure 5a shows the results of an instantaneous vector volume for α_{p1} with all measurement volumes combined. It should be pointed out that every position has been measured at different periods even so the characteristic vortex structures fit consistently. Shown are the isosurfaces of the normalized vorticity magnitude. The same vortical structures can be identified at α_{p2} in Figure 5b but enlarged in comparison to the smaller angle of attack. Figure 5c and 5d show phase-averaged vector volumes calculated using 141 samples. Two isosurfaces represent the normalized vorticity magnitude $|\omega_n| = 9.8$ and $|\omega_n| = 18$. The turbulent small scale flow structures are suppressed by averaging the results but especially the LEVs are not completely converged. A higher number of samples would have been necessary to smooth these structures. Nevertheless, the main vorticity structures are more obvious in phase-averaged representation. Regarding this structures for α_{p1} (Figure 5c) the tip vortex forms in a cone shape and changes its core structure to a douple helix to the rear part of the wing. This structure winds in a sense opposite to the direction of rotation of the tip vortex. The LEV is strongly influenced by the tip vortex. Close to the wing center the shear layer and the formed LEV can be seen. A secondary vortex is formed beneath the shear layer upstream the LEV that induces an upstream directed flow on the wing surface. A smaller vortex can be detected behind the wing of opposite sense of rotation of the LEV shedding form the trailing edge. This TEV is partially cropped by the boundary of the evaluation domain. Again the phase-averaged flow field of α_{p2} in Figure 5d shows basically the same vortices, i.e. LEV, TEV and tip vortex. The cone shaped part of tip vortex is expanded and changes its structure very abrupt at $x_n \approx 0.5$ to a small strong vortex tube. The TEV is now stronger and captured completely by the measurement domain for α_{p2}. The tip vortex influences the TEV by inducing a curved vortex core line. Regarding the near surface flow shown in Figure 6 a gap of 1.6 mm between model surface and vector volumes has to be considered. The slice has been extracted from the averaged volume data. The diverging streamlines indicate a flow reattachment line downstream the LEV. The separated region is larger in comparision to α_{p1}. Converging streamlines indicate a separation of the flow showing a secondary separation starting beneath LEV; this can be seen for α_{p1} and α_{p2} but stronger developed for α_{p2}. The focus point formed by the streamlines indicates the end points of the LEV on the surface.
Spanwise velocity components are shown in Figure 7 for both pitch angles. The slices have also been extracted from averaged volume data. A strong inboard flow inside the LEV core is visible which is more pronounced for α_{p2}. Close to the LE at outboard wing an outboard flow component is obvious. The TEV causes an outboard flow component, too. Regarding the extracted 2-D slices in detail minor inconsistencies are visible in regions of overlapping volumes. This may be caused by minimal imprecisions in the model motion over time. To measure all six volumes above the model taking in each case 150 samples took about 25 min. To avoid an overloading of the model actuation the motion had to be stopped and restarted some times.

5. Conclusion

The dominant vortex structures formed above a flat-plate wing performing a canonical pitch-up manoeuvre has been successfully measured by tomographic PIV. The measurement domain located directly on the upper side of the wind tunnel model was successively measured using six sub volumes to improve the spatial resolution of the measurement. For this, the set-up is shifted by high precision linear stages allowing for a scanning of the flow field in a chordwise direction. The complex evaluation was achieved within an acceptable time frame using DLR in-house software. Volume self-calibration is applied to correct occurring deviations. The reconstructed evaluation domain is resolved by ≈ 18.2 voxel/mm. A 3-D cross-correlation based algorithm is used to calculate the particle displacements. The 3-D flow fields show a strong spanwise dependency of the LEV caused mainly by the flow induced by the tip vortex. A strong inboard directed flow develops inside the LEV core. The extracted near surface flow gives information about flow separation and reattachment lines. Hence, a highly resolved data set is available now to study the vortex structures in more detail and to validate CFD codes.

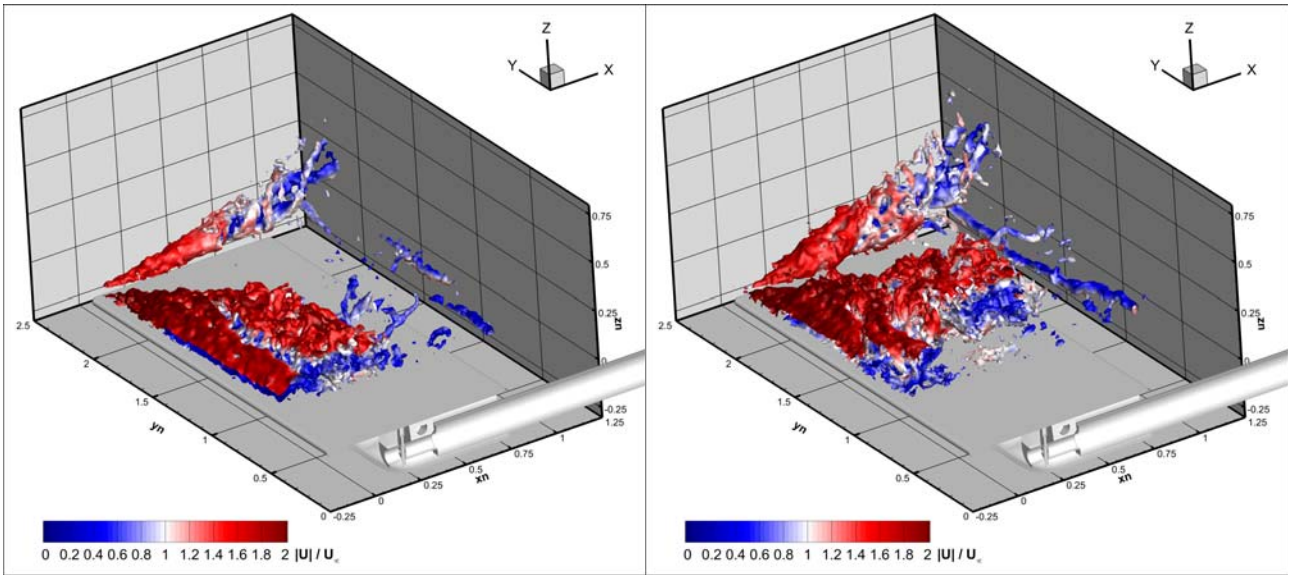

(a) instantaneous flow field for $\alpha_{p1} = 22.5°$; isosurface: $|\omega_n| = 22.8$.

(b) instantaneous flow field for $\alpha_{p2} = 30°$; isosurface: $|\omega_n| = 22.8$.

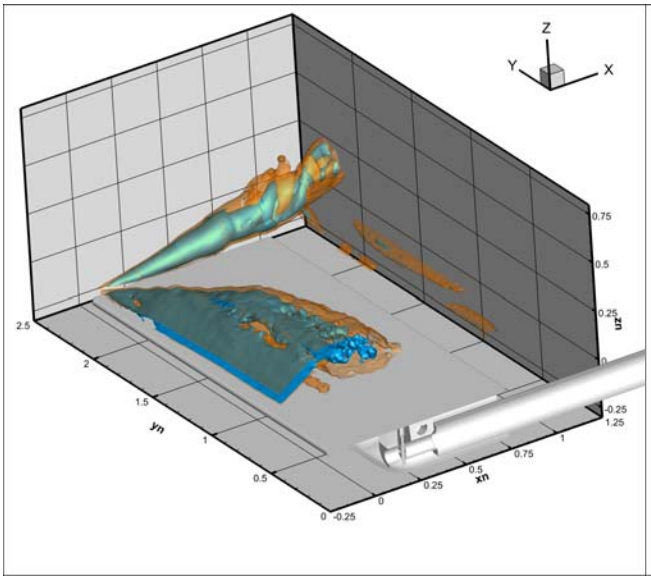

(c) averaged flow field for $\alpha_{p1} = 22.5°$; blue isosurface: $|\omega_n| = 9.8$, orange isosurface: $|\omega_n| = 18$.

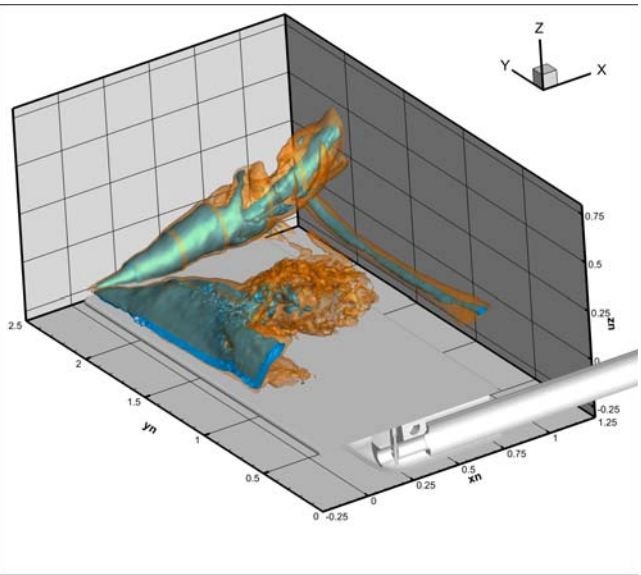

(d) averaged flow field for $\alpha_{p2} = 30°$; blue isosurface: $|\omega_n| = 9.8$, orange isosurface: $|\omega_n| = 18$.

Figure 5: 3-D flow fields measured by Tomo PIV; approaching flow from front left; first row: instantaneous flow fields; second row: phase-averaged flow fields (141 samples).

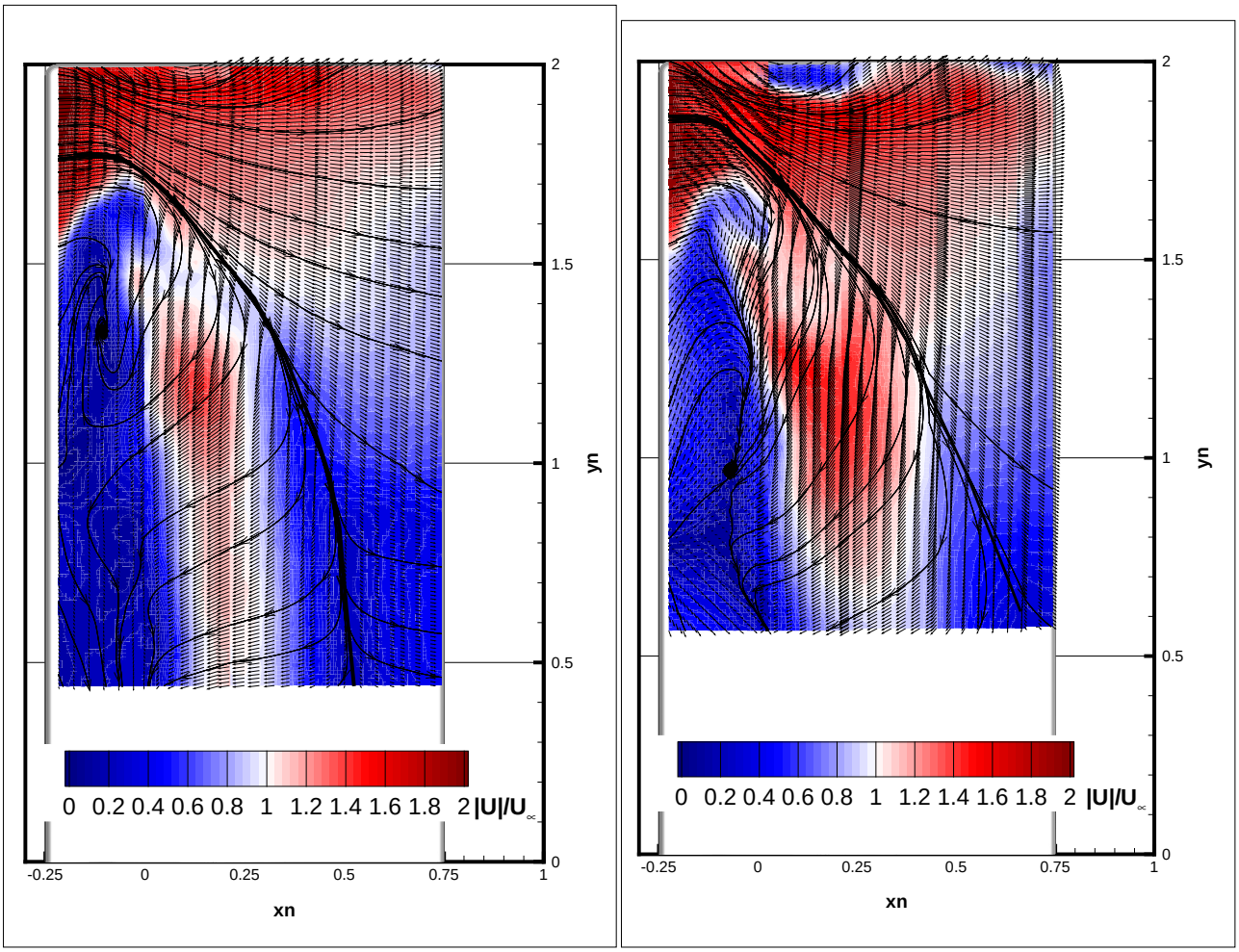

(a) near surface flow for $\alpha = 22.5°$.

(b) near surface flow for $\alpha = 30°$.

Figure 6: Near surface flow for both pitching angles colored by normalized velocity magnitude $|U|/U_\infty$; gap of 1.6 mm between model surface and evaluated volumes has to be considered; approaching flow from left to right; slices generated from phase-averaged flow field data.

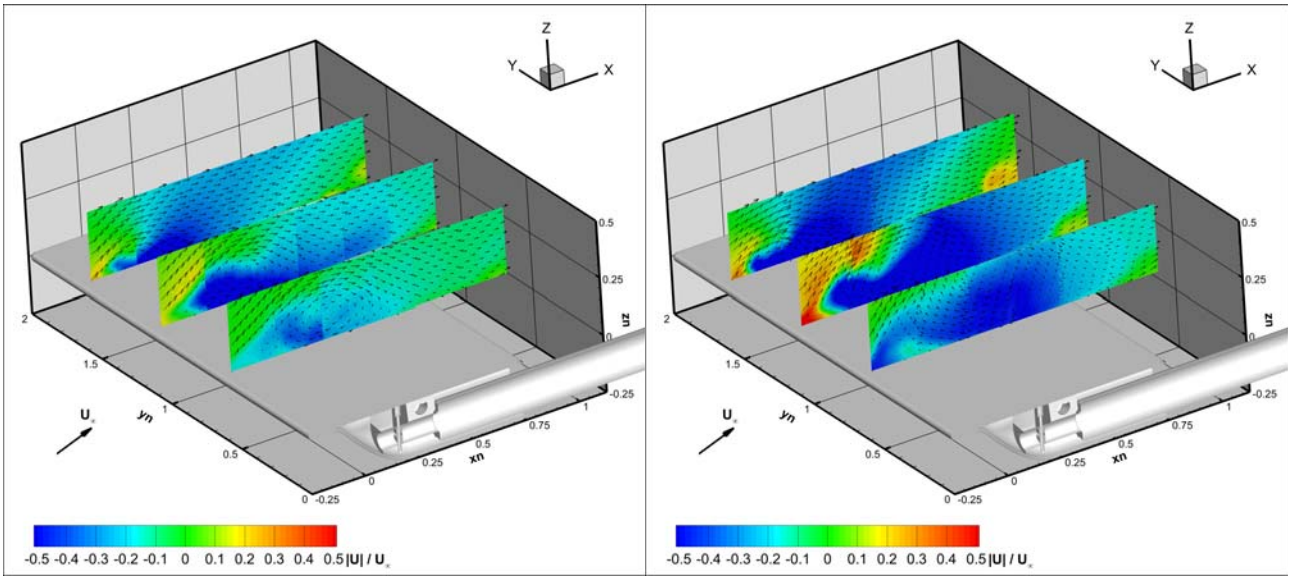

(a) v_n for $\alpha = 22.5°$.

(b) v_n for $\alpha = 30°$.

Figure 7: xz planes colored by normalized out-of-plane component of velocity v_n; approaching flow from front left; slices generated from phase-averaged flow field data.

REFERENCES

[1] Ol M and (Multiple) "Unsteady aerodynamics for micro air vehicles" Technical Report AVT 149, Research and Technology Organisation (2010)

[2] Lehmann FO "The mechanisms of lift enhancement in insect flight" Naturwissenschaften 91 (2004) pp. 101-122

[3] Visbal M, Yilmaz TO and Rockwell D "Three-dimensional vortex formation on a heaving low-aspect-ratio wing: Computations and experiments" Journal of Fluids and Structures 38 (2013) pp. 58-76

[4] Jantzen R, Taira K, Granlund G and Ol MV "On the Influence of Pitching and Acceleration on Vortex Dynamics Around Low-Aspect-Ratio Rectangular Wings" 51st AIAA Aerospace Sciences Meeting, 07 - 10 January (2013) AIAA 2013-0833

[5] Stevens PRRJ, Pitt Ford CW and Babinsky H "Experimental Studies of an Accelerating, Pitching, Flat Plate at Low Reynolds Number" 51st AIAA Aerospace Sciences Meeting, 07 - 10 January (2013) AIAA 2013-0677

[6] Elsinga G, Scarano F, Wieneke B and van Oudheusden BW "Tomographic Particle Image Velocimetry" Exp. Fluids 41 (2005) pp. 933-947

[7] Jones KD, Lund TC and Platzer MF "Experimental and Computational Investigation of Flapping Wing Propulsion for Micro Air Vehicle" In: Müller, TJ (ed.): Fixed and Flapping Wing Aerodynamics for Micro Air Vehicle Applications. Vol. 195, AIAA-Reihe: Progress in Astronautics and Aeronautics (2001) pp. 307-339

[8] Wokoeck R, Radespiel R, Ehlers H and Konrath R "Experimental and numerical investigations of pitch-plunging wing aerodynamics at low Reynolds number" International Journal of Engineering Systems Modelling and Simulation, Vol. 5, No. 1/2/3 (2013) pp. 19-32

[9] Wieneke B "Volume self-calibration for StereoPIV and Tomographic PIV" Exp. Fluids 45 (2007) pp. 549-556

[10] Atkinson C and Soria J "An efficient simultaneous reconstruction technique for tomographic particle image Velocimetry" Exp. Fluids 47 (2009) pp. 563-578

[11] Schanz D, Gesemann S, Schröder A, Wieneke B and Novara M "Non-uniform optical transfer functions in particle imaging: calibration and application to tomographic reconstruction" Meas. Sci. Technol. 24: 024009 (2013)

[12] OpenMP Architecture Review Board "OpenMP Application Program Interface Version 3.1" (2011) `http://www.openmp.org/mp-documents/OpenMP3.1.pdf`

[13] Thévenaz P, Blu T and Unser M "Interpolation Revisited" IEEE Transactions on Medical Imaging Vol. 19, No. 7 (2000) pp. 739-758

[14] Raffel M, Willert C, Wereley S and Kompenhans J "Particle Image Velocimetry, A Practical Guide" Springer Berlin-Heidelberg (2007)

[15] Scarano F “Iterative image deformation methods in PIV” Measurement Science and Technology Vol. 13, No. 1 (2002)

[16] Discetti S and Astarita T “Fast 3D PIV with direct sparse cross-correlations” Exp. Fluids 53, No. 5 (2012) pp.1437-1451

[17] Wereley ST and Meinhart CD “Second-order accurate particle image velocimetry” Exp. Fluids 31, No. 3 (2001) pp.258-268

[18] Westerweel J, Dabiri D and Gharib M “The effect of a discrete window offset on the accuracy of cross-correlation analysis of digital PIV recordings” Exp. Fluids 23, No. 1 (1997) pp. 20-28

[19] Westerweel J and Scarano F “Universal outlier detection for PIV data” Exp. Fluids 39, No. 6 (2005) pp. 1096-1100

[20] Frigo M and Johnson SG “The Design and Implementation of FFTW3” Proceedings of the IEEE Vol. 93, No. 2 (2005) pp. 216-231